MOLECULAR IMAGING AND BIOLOGY
Mol Imaging Biol (2013) 15:655–665
DOI: 10.1007/s11307-013-0656-5

RESEARCH ARTICLE

Respiratory-Induced Errors in Tumor Quantification and Delineation in CT Attenuation-Corrected PET Images: Effects of Tumor Size, Tumor Location, and Respiratory Trace: A Simulation Study Using the 4D XCAT Phantom

Parham Geramifar,[1] Mojtaba Shamsaie Zafarghandi,[1] Pardis Ghafarian,[2,3]
Arman Rahmim,[4] Mohammad Reza Ay[5,6,7]

[1] *Faculty of Nuclear Engineering and Physics, Amirkabir University of Technology, Tehran, Iran*
[2] *Chronic Respiratory Disease Research Center, NRITLD, Masih Daneshvari Hospital, Shahid Beheshti University of Medical Sciences, Tehran, Iran*
[3] *Telemedicine Research Center, NRITLD, Masih Daneshvari Hospital, Shahid Beheshti University of Medical Sciences, Tehran, Iran*
[4] *Department of Radiology, Johns Hopkins University, Baltimore, MD, USA*
[5] *Medical Imaging Group, Research Center for Molecular and Cellular Imaging, Tehran University of Medical Sciences, Tehran, Iran*
[6] *Research Center for Nuclear Medicine, Tehran University of Medical Sciences, Tehran, Iran*
[7] *Department of Medical Physics and Biomedical Engineering, Tehran University of Medical Sciences, Tehran, Iran*

Abstract

Purpose: We investigated the magnitude of respiratory-induced errors in tumor maximum standardized uptake value (SUV_{max}), localization, and volume for different respiratory motion traces and various lesion sizes in different locations of the thorax and abdomen in positron emission tomography (PET) images.

Procedures: Respiratory motion traces were simulated based on the common patient breathing cycle and three diaphragm motions used to drive the 4D XCAT phantom. Lesions with different diameters were simulated in different locations of lungs and liver. The generated PET sinograms were subsequently corrected using computed tomography attenuation correction involving the end exhalation, end inhalation, and average of the respiratory cycle. By considering respiration-averaged computed tomography as a true value, the lesion volume, displacement, and SUV_{max} were measured and analyzed for different respiratory motions.

Results: Respiration with 35-mm diaphragm motion results in a mean lesion SUV_{max} error of 24 %, a mean superior inferior displacement of 7.6 mm and a mean lesion volume overestimation of 129 % for a 9-mm lesion in the liver. Respiratory motion results in lesion volume overestimation of 50 % for a 9-mm lower lung lesion near the liver with just 15-mm diaphragm motion. Although there are larger errors in lesion SUV_{max} and volume for 35-mm motion amplitudes, respiration-averaged computed tomography results in smaller errors than the other two phases, except for the lower lung region.

Conclusions: The respiratory motion-induced errors in tumor quantification and delineation are highly dependent upon the motion amplitude, tumor location, tumor size, and choice of the attenuation map for PET image attenuation correction.

Key words: Respiratory motion artifact, PET/CT, Tumor quantification, SUV, CTAC

Correspondence to: Mohammad Ay; *e-mail:* mohammadreza_ay@tums.ac.ir

Introduction

Due to increasing availability of integrated positron emission tomography (PET)/computed tomography (CT) units, CT is now commonly used for PET image attenuation correction (AC). Among the advantages of CTAC over radionuclide transmission scans are the generation of noise-free attenuation map, faster scan time, and ability to collect uncontaminated postinjection transmission scan [1–3]. However, CTAC increases the patient radiation dose and suffers from a number of other drawbacks [4–6]. The fast data acquisition of CT, compared to PET, creates data inconsistencies leading to tumor mislocalization and overestimation of tumor volume. Furthermore, it may bias the PET tracer distribution following CTAC and becomes a major source of error in tumor quantification such as maximum standardized uptake value (SUV_{max}) that is typically used in clinical practice [7–9].

The comparison of CTAC PET images with those attenuation corrected using the radionuclide transmission source also allows evaluation of the fusion and lesion localization accuracy and the severity of respiration motion-induced errors, as it is assumed the radionuclide transmission image has the same temporal resolution and the same diaphragm average position as the PET image [7, 10–15]. In these studies, a SUV bias in normal tissues, especially when CT was acquired during inspiration, has been reported.

Several investigators quantitatively evaluated respiratory-induced motion of lung lesions [7, 10, 13, 16–21]. The motion during the respiratory cycle was characterized using gated acquisition or by analysis of lesion displacement in PET versus CT images. In those studies, the lung lesions' motion amplitude varied from 4 to 25 mm depending on the lesion location, and the average displacement was larger in the lower lung region. Furthermore, the motion amplitudes were more significant in the superior inferior direction than the anterior posterior direction, which themselves exceeded those in the left–right direction [22, 23]. Depending on the lesion size, the lesion volume overestimation was varied from 24 to 93 % [7, 8]. Errors in the localization of lung versus liver tumors were also investigated, and displacement of liver lesion into the right lower lung was observed as attributed to the respiratory motion [14, 24].

It has been shown that respiratory motion-induced blurring in PET imaging reduces the measured SUVs in lung tumors. Furthermore, an increase of SUV_{max} ranging from 7 to 159 % was observed when analyzing only a single phase in a gated study as a result of the reduction in the lesion volume [25]. As a result of a phantom study reproducing conditions of gated PET, respiratory blurring may underestimate SUV by 21 to 45 % depending on the lesion size [17]. There are other phantom studies evaluating the SUV_{max}, but due to the simple and nonrealistic oscillatory motion for driving the phantom movements, these studies do not capture the variation in respiratory motion patterns [26, 27].

In another study [28], the mean ratio of lesion SUV to normal liver SUV in some liver dome metastases was compared between the CTAC- and cesium-based AC PET images with SUV ratios of 0.81 and 1.51, respectively. The sensitivity of PET may be reduced by such an underestimation, especially for small lesions exhibiting mild hypermetabolism [29].

While there is no optimal respiratory protocol as a standard for PET/CT imaging, the most often proposed protocol is breathing involving holding the breath at the end of a normal exhalation [18, 30–33]. Even with substantial breath coaching, it is difficult to state the optimal breath protocol applicable to all patients. In a study that investigated misalignments between CT and PET, holding the breath in midexpiration results in misalignments in 50 out of 100 subjects, exceeding 20 mm in 34 subjects [21].

Simulations have been proven useful to evaluate parameters of interest and quantification methods in PET imaging [34–42]. The availability of the ground truth is the advantage of using simulated data compared to clinical data; however, the simulated images should be sufficiently realistic to allow conclusions to be extrapolated to clinical PET images. In PET tumor imaging, extensively used simulation methods are Monte Carlo [35–40] and computational anthropomorphic anatomical and physiological models, such as the XCAT phantom [41] or the Zubal phantom [42] based on real clinical data. Zaidi et al. reviewed computational anthropomorphic anatomical and physiological models [43]. Accurate modeling of heterogeneous physiological uptake remains challenging in these phantoms as the activity concentration to be assigned to each region has to be fixed [41, 42].

Although respiratory-induced errors in tumor quantification of CTAC PET images have, no doubt, been documented, a study of combined effects of tumor size, tumor location, respiratory trace and diaphragm motion with their impact on tumor quantification, and delineation appears to be missing and is needed to shed light on the combinative effects of these factors. In this study, we investigated the impact of respiratory motion on tumor quantification and delineation for various lesion sizes in different locations of the thorax and abdomen. Using the 4D XCAT phantom, we simulated a common patient respiratory trace and different diaphragm motions, and used three phases of CT breathing cycle, end exhalation (EE), end inhalation (EI), and respiration-averaged CT (ACT) for PET image attenuation correction. By considering ACT as a true value, we investigated the magnitude of induced errors in tumor SUV_{max}, localization, and volume for other breathing phases aiming to arrive at a more complete understanding of the respiratory motion artifacts in PET/CT imaging of the thorax.

Materials and Methods

4D XCAT Phantom

Simulation studies were performed using the 4D XCAT phantom, a realistic whole-body computer model based on nonuniform rational B-spline surfaces (NURBS) representing the human anatomy and physiology [41]. This voxelized model generates attenuation and activity maps at the same time with any desired biodistribution, and using high-resolution respiratory-gated CT datasets realistically model the respiratory motion in the body. The motion of the lung, heart, liver, abdominal organs, and diaphragm involved in respiration were incorporated into the 4D XCAT phantom. The attenuation maps generated at 511 keV were used for attenuation correction in image reconstruction. Activity maps in the abdomen and thorax with the corresponding attenuation maps were used to assess respiratory motion-induced errors on the reconstructed CTAC PET images. To correctly interpret the PET/CT study, normal organ 2-deoxy-2-[^{18}F]fluoro-D-glucose (FDG) activity concentrations were calculated from the SUV measurements in the literatures [44, 45] as listed in Table 1. In our study, ten emission and related attenuation images were produced in a normal respiratory cycle of 5 s and, subsequently, each image corresponded to 0.5 s within a cycle. The matrix size of all images (both activity and attenuation maps) was 128×128 with a pixel size of 3.125 mm.

Lesion Size, Location, and Activity

Poor spatial resolution of conventional PET scanners and the respiratory motion blurring result in missing small lung lesions in diagnosis, especially with low uptake. As a result, physicians are recommended to use PET to characterize lesions not smaller than ~10 mm in diameter [46, 47]. As we aim to investigate how lesion size affects the quantification, various lesion sizes of 9, 15, 21, and 27 mm in diameter were simulated in different locations of the thorax as shown in Fig. 1. The lesions were placed at the (i) top of the liver; (ii) upper, (iii) middle, and (iv) lower lobes of the right lung; and (v) middle lobe of the left lung based on consultation with physicians in our department. A lesion to organ activity ratio of 8:1 was used in all simulations. It should be noted that other groups have used nearly similar ratios in simulation [48–50].

Respiratory Pattern and Diaphragm Motions

The respiratory motion pattern was simulated based on a classification of respiratory traces in a study performed at the University of Washington Medical Center [49]. The investigators acquired 1,295 respiratory traces (using the Varian RPM system), acquired from about 70 % male and 30 % female patients, each representing about 8-min natural free breathing during the PET/CT study. Each trace was classified into one of three types (type 1, type 2, and type 3) according to the qualitative shape of the displacement histogram. There is a distinguished peak at the low end of the displacement histogram in type 1 trace due to the fact that the patient's breathing cycle tends to spend more time near end exhalation and consistently returns to a similar location as confirmed by other studies [10, 51] .There are numerous respiratory patterns in the Gaussian- or Poisson-like histogram of type 2 trace like variable end-exhalation locations or similar inhalation and exhalation phase lengths. There is no recognizable shape in the type 3 histogram due to the long-term variability of the respiratory traces and is simply spread out over the histogram bins. Type 1, type 2, and type 3 traces account for about 60, 20, and 20 % of the studied patient respiratory traces, respectively. Considering ~5 min for CT scan and preparation, we used the type 1 respiratory signal in the abovementioned work from the reference point of 300 s and scaled it to three normal diaphragm motion amplitudes of 15, 25, and 35 mm for right and left diaphragms in such a way that their displacement histograms mimicked the type 1 motion trace as shown in Fig. 2. The simulated diaphragm motion amplitudes, determined as the maximum displacement of the diaphragms (left and right) in the 4D XCAT phantom, are consistent with other published studies [52, 53].

Table 1. Radioactivity concentrations of organs, calculated from SUV measurements in the literature [44, 45]

Organ	Radioactivity concentration (Bq/cc)
Background	2,000
Myocardium	10,000
Spleen	7,000
Liver	7,800
Lung	1,600
Stomach	6,500
Liver lesion	62,400
Lung lesion	12,800

Attenuation Correction and PET Image Reconstruction

Attenuation correction and reconstruction of PET images were performed using Software for Tomographic Image Reconstruction (STIR) [54]. The 511-keV attenuation maps were applied to model attenuation within the data simulation. In order to analytically generate sinograms from the XCAT output images, the STIR ray tracing technique [54] was used to accurately calculate projections directly from the XCAT phantom using parameters defining the sensitivity, depth of interaction, and geometry of the ECAT EXACT HR+ (CTI/Siemens Knoxville). This scanner has 55 rings with 672 detectors per ring and eight crystals per block in both axial and transaxial directions. The inner ring diameter is 82.5 cm with 0.675 cm distance between the rings. The average depth of interaction and the default bin size were set to 0.7 and 0.675 cm respectively. Also, an effective central bin size of 0.342 cm was used. Using the single scatter simulation formula as implemented in STIR, the effect of scatter was simulated analytically.

After forward projection, the generated sinograms including attenuation modeling (as properly performed distinctly for each respiratory gate) were then attenuation corrected using the CTAC procedure for the EE CT (PET/EECT), the EI CT(PET/EICT), and the average of the respiratory cycle (PET/ACT) to study how the choice of the attenuation map affects reconstructed CTAC PET images. The attenuation coefficient factors (ACF) of the attenuation maps generated using forward projections were used in the process of attenuation modeling and correction. The ordered subsets expectation maximization (OSEM) algorithm, as routinely employed in commercial reconstruction software, was used for the reconstruction of the PET images involving four iterations and 20 subsets. Reconstruction of each gate takes ~10 min on a personal computer with a 3.30 GHz CPU and 8 GB RAM.

Assessment Strategy

The motion-blurred sinograms were simulated for four lesion sizes in five different locations of the abdomen and thorax, with 8:1 contrast. Meanwhile, a common patient respiratory trace (type 1) was scaled to

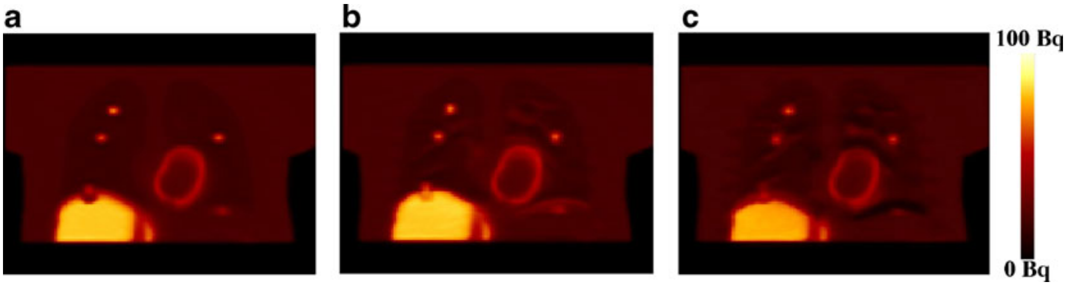

Fig. 1. Sample XCAT simulation of 15-mm lesions in different locations of the thorax driven by 35-mm type 1 diaphragm motion. The reconstructed coronal slices were attenuation corrected using **a** the respiration-averaged CT (ACT) and misaligned CT images: **b** end-exhalation CT (EECT) and **c** end-inhalation CT (EICT). The impact of respiratory motion artifact is significant at the diaphragm level. The artifact was reduced in the PET/ACT.

three diaphragm motion amplitudes of 15, 25, and 35 mm to study the impact of different motions on tumor quantification. The generated PET sinograms were then attenuation corrected using EECT, EICT, and ACT. By considering ACT as the true value [21], we investigated the magnitude of induced errors on tumor delineation in terms of tumor volume, displacement, and quantification in terms of $\mathrm{SUV}_{\max}$, for the other phases of breathing cycle. It should be noted that the stationary (no respiratory motion) PET/CT image was also reconstructed as the "stationary truth" value for the quantification of all lesions, especially for small lower lung lesions where ACT-based reconstructions shows larger errors and prevented meaningful volume measurements around the liver dome.

For lesion quantification, the SUV value is calculated using Eq. (1), with the injected FDG dose of 370 MBq and the phantom weight of 95.0 kg:

$$\mathrm{SUV} = \frac{\text{FDG activity concentration (MBq/ml)}}{\text{Injected dose (MBq)/phantom weight (g)}}. \tag{1}$$

The lesion $\mathrm{SUV}_{\max}$, measured using the maximum voxel value of the lesion, was used for quantitative evaluation. For each PET/EECT- and PET/EICT-reconstructed image, the change of lesion $\mathrm{SUV}_{\max}$ with respect to that of the PET/ACT was analyzed as:

$$\Delta\mathrm{SUV}_{\max} = \frac{\mathrm{SUV}_{\max} - \mathrm{SUV}_{\mathrm{PET/ACT}}}{\mathrm{SUV}_{\mathrm{PET/ACT}}} \tag{2}$$

where $\mathrm{SUV}_{\mathrm{PET/ACT}}$ denotes the lesion $\mathrm{SUV}_{\max}$ measured from the PET/ACT image, and $\mathrm{SUV}_{\max}$ denotes the values obtained from either PET/EECT or PET/EICT images. As such, respiratory motion artifacts inducing errors in quantification accuracy were determined using the abovementioned $\Delta\mathrm{SUV}_{\max}$ metric. To investigate the respiratory-induced errors in lesion volume estimation and localization, a threshold strategy was used for defining the regions of interest (ROIs). As accurate tumor volume estimation is critical in radiation treatment planning and treatment response monitoring, several studies have tried different threshold settings of $\mathrm{SUV}_{\max}$ with the aim of finding the optimized voxel intensity for gross tumor volume contouring [55, 56]. Therefore, we used the threshold setting of 20 % maximum voxel intensity, as it achieves the optimal correlation of volume ratio, tumor length, and conformity index in 4D-PET/CT images [56]. For each PET/EECT- and PET/EICT-reconstructed image, the change of lesion volume with

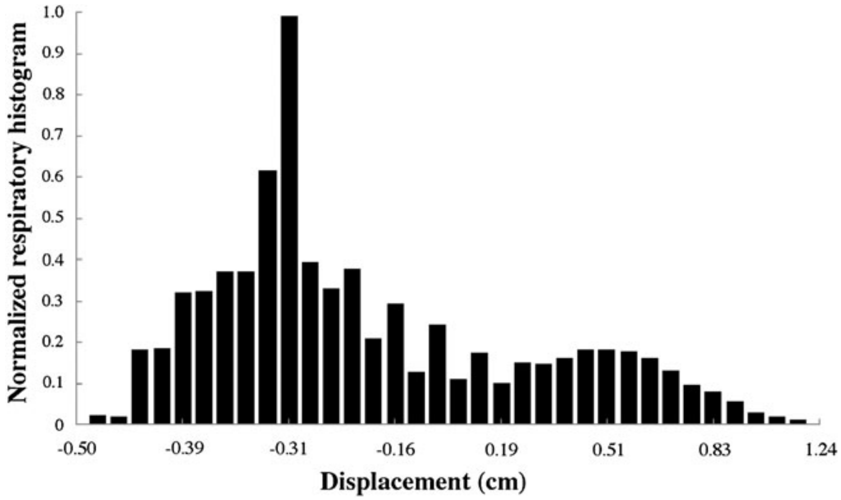

Fig. 2. Normalized respiratory histogram based on common patient breathing cycle. The data simulated from the study done at University of Washington Medical Center [49].

respect to that of the PET/ACT was measured using the equation as follows:

$$\Delta V = \frac{V' - V_{\mathrm{PET/ACT}}}{V_{\mathrm{PET/ACT}}} \quad (3)$$

where $V_{\mathrm{PET/ACT}}$ denotes the lesion volume measured using the threshold at 20 percentage of the lesion $\mathrm{SUV}_{\max}$ in the PET/ACT image and V' denotes the lesion volume obtained from either PET/EECT or PET/EICT images using the same threshold. The centroid voxel of the lesion volume was then utilized for measuring respiratory-induced displacements during the breathing cycle. The centroid voxels were defined via manual analysis of a human expert.

Results

Lesion Displacement

Respiratory-induced lesion motion varied dramatically for different respiratory patterns, lesion sizes, and locations. The lesion centroid shifts in PET/ACT images compared with the stationary truth are shown as a radar plot in Fig. 3 for 20 lesions (four sizes and five locations). For all lesions, the Euclidean distance in the anterior–posterior (AP) and superior–inferior (SI) directions was used as a displacement measure between the centroids. The medial–lateral (ML) (i.e., right–left) direction was not included in the measurements due to negligible displacements. The lesion centroid shifts are shown in triangles, squares, and circles for diaphragm motions of 15, 25, and 35 mm, respectively. It is clearly seen that the lower lung lesion depicts the largest discrepancies up to 6–7 mm due to respiratory motion. In particular, the maximum lesion centroid shift was 6.9 mm for the 27-mm lower lung lesion with 35-mm diaphragm motion.

Figure 4 shows the lesion centroid shift in PET/EECT and PET/EICT compared with PET/ACT in both the SI and AP directions. The displacement in the ML direction was not analyzed in detail because the maximum extent was less than 3.1 mm. The lesion centroid shifts, measured for the type 1 respiratory pattern, are shown in black- and gray-colored columns for diaphragm motions of 15 and 25 mm, respectively, and in dark diagonal pattern column for diaphragm motion of 35 mm, respectively. The results of the comparison between PET/EECT and PET/ACT are shown in Fig. 4a and b for SI and AP directions, respectively. The maximum lesion centroid shift was 7.6 mm in the SI direction and 3.8 mm in the AP direction with 35-mm diaphragm motion for 9-mm liver lesions. The lesion displacements were larger for the lower lung region in comparison with the middle and upper lung regions, except for the 9-mm lesion with 35-mm diaphragm motion as the centroid shift was not measurable due to the blurring. Both the liver lesions and the small lower lobe lesions were the ones most affected by respiratory motion, in general. A similar trend was observed for the displacement in the AP direction.

Figure 4c and d shows the results of the comparison between PET/EICT and PET/ACT. The maximum lesion centroid shift in the SI direction was 10.2 and 8.1 mm for the 9-mm liver lesion and 15-mm lower lung lesion, respectively. The maximum displacement in the AP direction was 4.2 mm for 15 mm lower lung lesion with 35-mm diaphragm motion.

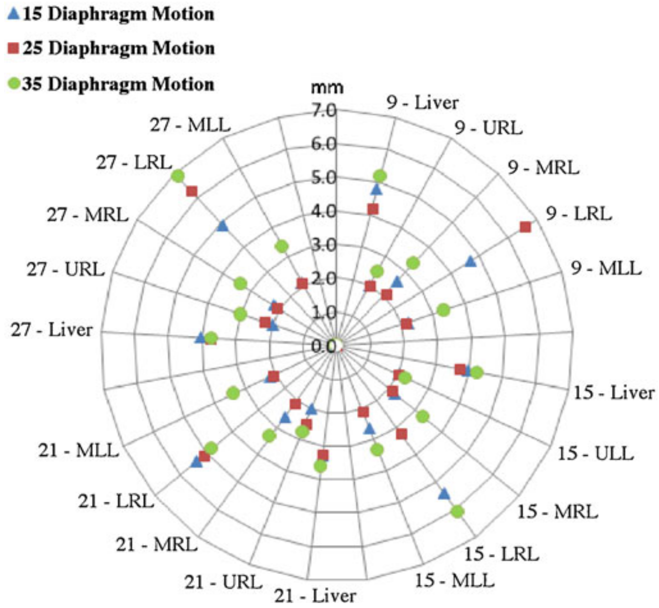

Fig. 3. Radar plot of lesion centroid shift (mm) due to the respiratory motion in PET/ACT image compared with stationary truth. For all lesions, the Euclidean distance in SI and AP directions was used as a displacement measure between centroids. *URL* Upper lobe in the right lung, *MRL* middle lobe in the right lung, *LRL* lower lobe in the right lung, *MLL* middle lobe in the left lung. *Triangles*, *squares*, and *circles* denote diaphragm motions of 15, 25, and 35 mm, respectively.

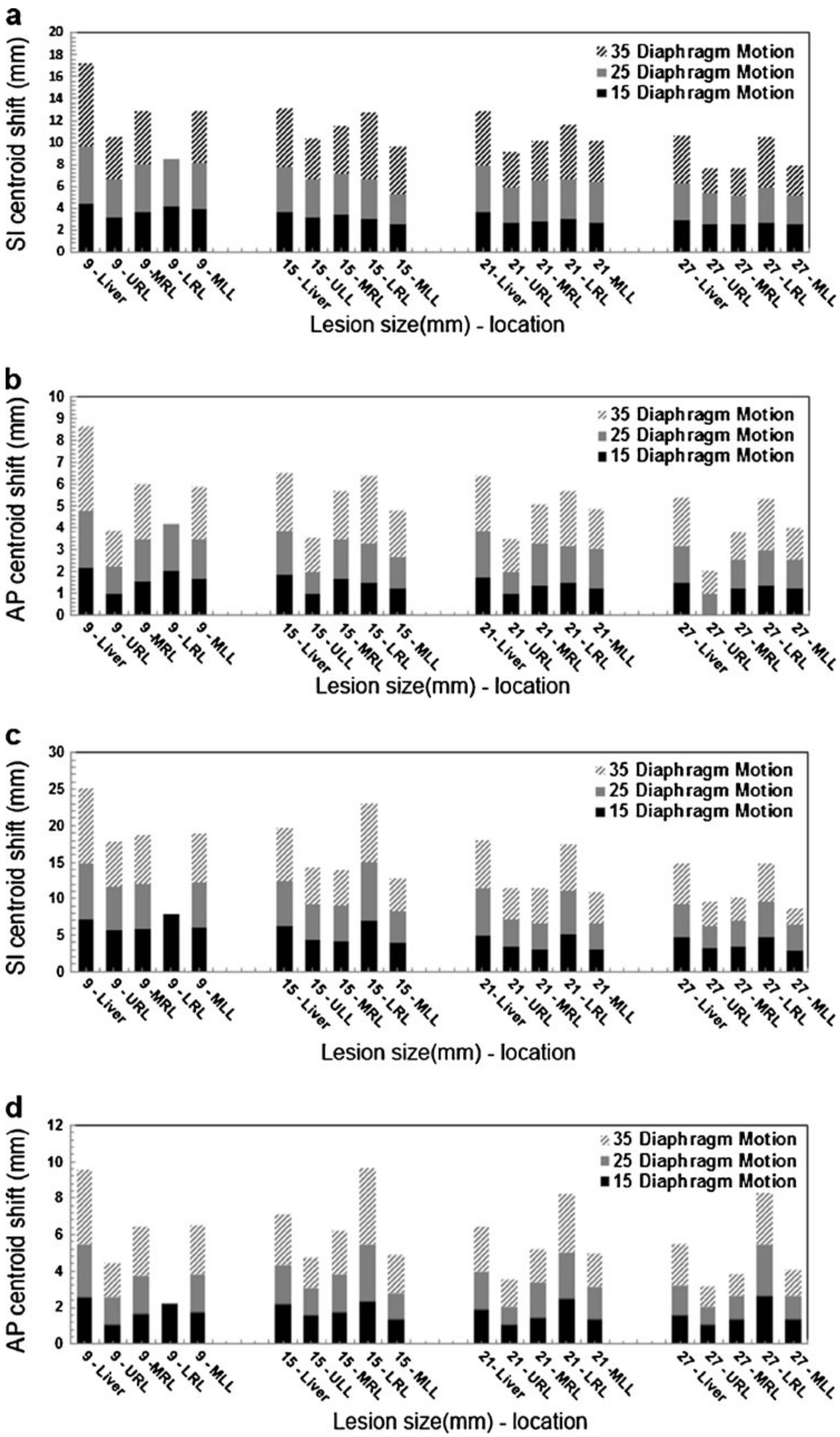

Fig. 4. Displacement of lesions (mm) due to the respiratory motion in **a** SI and **b** AP directions in PET/EECT image compared with PET/ACT. The induced centroid shift in SI and AP directions in PET/EICT image compared with PET/ACT are shown in **c** and **d**, respectively. *URL* Upper lobe in the right lobe, *MRL* middle lobe in the right lung, *LRL* lower lobe in the right lung, *MLL* middle lobe in the left lung. The *black- and gray-colored columns* with the *dark diagonal pattern column* denote diaphragm motions of 15, 25, and 35 mm, respectively.

Again, the centroid shift was not measurable due to the blurring for 9-mm lesion in the lower lobe in both 25- and 35-mm diaphragm motions.

Lesion Volume Measurement

Table 2 shows the percentage errors of lesion volume measurements in PET/EECT, PET/EICT, and stationary truth compared with PET/ACT for different lesion locations, lesion sizes, and diaphragm motion amplitudes. Lesion volumes were measured with thresholds at 20 % maximum voxel intensity for type 1 respiratory pattern. Comparing stationary truth with PET/ACT, the volume measurement errors were increased in a trend of larger errors for higher diaphragm motions, in general. The upper lung lesion volume measurements show a maximum 3 % overestimation in PET/ACT, while in the middle lobe, the maximum percentage error was 11 %. Furthermore, lower lung lesions exhibit larger percentage errors, up to a maximum of 157 % overestimation in the 9-mm lesion with 35-mm diaphragm motion. Finally, the amplitudes of errors for liver lesions were between −19 and −47 %. Comparing PET/EECT and PET/EICT with PET/ACT, for the five lesion locations shown in Table 2, the percentage error was increased in a trend of larger errors for smaller lesions, with the exception of the lower lobe and upper lobe regions, neither of which showed a clear trend. The upper lung lesion volume measurements show smaller percentage fluctuations but no clear trend. The middle and upper lobe lesion volume measurements contain the smallest percentage errors. However, liver lesions exhibit more error for smaller lesions and higher diaphragm motions. The maximum percentage error, i.e., volume overestimation, was 129 % for the 9-mm liver lesion with 35-mm diaphragm motion. Finally, as shown in Table 2, the amplitudes of errors were relatively more prominent for middle lobes for the right lung in comparison to the left lung. Again, the PET/EICT measurements gave the largest volume error, in general.

Lesion SUV_{max}

Figure 5 shows the measurements of lesion ΔSUV_{max} in PET/ACT in comparison with the stationary truth, and Fig. 6a and b shows the measurements of lesion ΔSUV_{max} in PET/EECT and PET/EICT, respectively, in comparison with PET/ACT using Eq. 2. The changes in SUV_{max} were measured and analyzed for 20 lesions in three diaphragm motion amplitudes. Comparing stationary truth (no motion) PET/CT image with PET/ACT, as shown in Fig. 5, SUV_{max} error for the upper lung lesions was slightly smaller. However, the trend is reversed for the lower lung and liver lesions, showing larger errors with maximum SUV_{max} errors of 47 and 37 %, respectively.

As shown in Fig. 6a, ΔSUV_{max} for PET/EECT in both the liver regions and the middle and upper lung regions has negative values, while it does not show a trend for the lower lung lesions. The results show generally larger values for the lesions closer to the diaphragm, while for the upper lung lesions, the values do not show significant changes. Figure 6b shows that PET/EICT resulted in further SUV_{max} underestimation, especially for liver lesions and, to some extent, for the lower lung lesions. Spending more time at expiration in PET/ACT makes ΔSUV_{max} smaller in PET/EECT compared to PET/EICT. The largest mean SUV_{max} error was ~30 % related to the liver lesions with 9-mm diaphragm motion. Lesions with 21- and 27-mm diameters lead to smaller ΔSUV_{max}, indicating that respiratory-induced motion errors are more significant for larger lesions than smaller lesions.

Table 2. Lesion volume errors of PET/EECT, PET/EICT, and stationary truth (ST) compared with PET/ACT for different diaphragm motions, lesion locations, and sizes. Volumes are measured with thresholds at 20 % maximum voxel intensity

Lesion size (mm)	Attenuation map	Lesion location														
		Liver			URL			MRL			LRL			MLL		
		A	B	C	A	B	C	A	B	C	A	B	C	A	B	C
9	EE	94 %	82 %	129 %	6 %	1 %	6 %	48 %	24 %	43 %	−5 %	9 %	18 %	21 %	19 %	19 %
	EI	12 %	43 %	122 %	11 %	8 %	8 %	50 %	32 %	26 %	50 %	9 %	9 %	26 %	16 %	12 %
	ST	−32 %	−40 %	−47 %	−1 %	−2 %	−2 %	−9 %	−7 %	−7 %	−62 %	−95 %	−157 %	−5 %	−6 %	−6 %
15	EE	36 %	41 %	78 %	−3 %	−11 %	−5 %	31 %	34 %	29 %	9 %	−10 %	−7 %	12 %	12 %	14 %
	EI	26 %	36 %	25 %	3 %	10 %	−3 %	28 %	30 %	60 %	2 %	24 %	−4 %	12 %	24 %	8 %
	ST	−29 %	−38 %	−43 %	−2 %	−1 %	−3 %	−8 %	−8 %	−11 %	−68 %	−102 %	−128 %	−5 %	−6 %	−9 %
21	EE	32 %	42 %	40 %	1 %	5 %	14 %	3 %	9 %	8 %	5 %	5 %	21 %	6 %	15 %	8 %
	EI	31 %	3 %	30 %	1 %	4 %	5 %	5 %	16 %	30 %	0 %	22 %	33 %	11 %	22 %	30 %
	ST	−27 %	−32 %	−42 %	−2 %	−2 %	−2 %	−9 %	−7 %	−9 %	−83 %	−108 %	−137 %	−6 %	−8 %	−8 %
27	EE	22 %	26 %	24 %	8 %	8 %	10 %	16 %	4 %	10 %	1 %	−4 %	1 %	15 %	3 %	10 %
	EI	21 %	20 %	3 %	8 %	−2 %	−9 %	25 %	16 %	5 %	8 %	−1 %	4 %	25 %	16 %	5 %
	ST	−19 %	−21 %	−34 %	−1 %	−2 %	−2 %	−8 %	−9 %	−9 %	−74 %	−140 %	−135 %	−7 %	−7 %	−9 %

A, B, and C represent 15-, 25-, and 35-mm diaphragm motion amplitudes

URL Upper lobe in the right lung, *MRL* middle lobe in the right lung, *LRL* lower lobe in the right lung, *MLL* middle lobe in the left lung

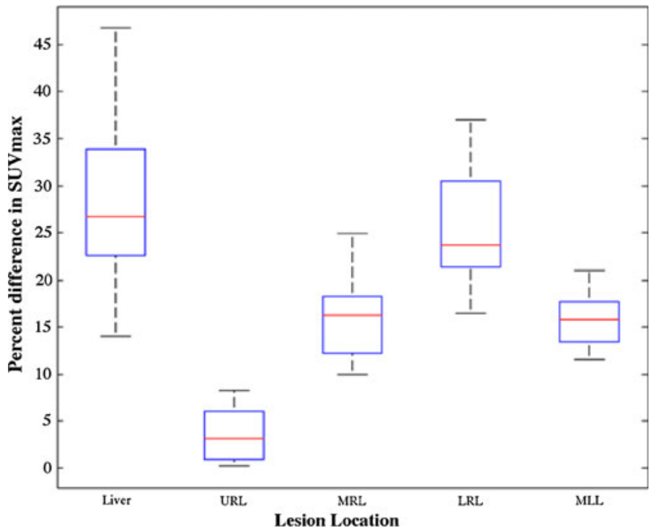

Fig. 5. *Box plots* of the ΔSUV_{max} for different lesion locations in PET/ACT images compared with the stationary truth. *URL* Upper lobe in the right lung, *MRL* middle lobe in the right lung, *LRL* lower lobes in the right lung, *MLL* middle lobe in the left lung. The *box* stretches from the lower 25 % quartile to the upper 75 % quartile with a *line across the box* representing the median. *Whiskers* extend from each end of the box to the most extreme values in the data within 1.5 times the interquartile range, which is defined as the difference between the upper quartile and the lower quartile, from each end of the box. Outliers with values beyond the ends of the whiskers are displayed with a *plus sign*.

Discussion

Monte Carlo (MC) simulations provide "the golden standard" in simulation techniques, themselves providing a reference truth for various studies [35, 37–39]. However, our experience has shown that analytic simulations, with appropriate modeling, have attractive advantages and can provide reliable results, allowing efficient simulations of a remarkable combination of activities and organ/tumor sizes and positions, which the computational intensity of MC methods may prevent. Ultimately, whether utilizing analytic or MC simulations, one ought to recognize that the complexity of the real world defies exact replication and that any technique arrived at, and/or optimized, via simulation methods in the virtual domain ought to be evaluated in the real domain.

Lesion displacement was most pronounced in the SI direction, especially for lesions near the diaphragm dome with higher diaphragm motions. Prior studies [7, 13, 22] presented a similar result; however, they did not investigate the impact of respiratory pattern and the applied attenuation map, which may have affected the results in some locations. As Fig. 3 shows, with the exception of lower lobe lesions, the lesion displacements were less than 3.5 mm, and ACT could be effective in removing misregistration artifacts, in general. Comparing PET/EECT and PET/EICT with PET/ACT, less displacement was exhibited in the former mainly because exhalation is the longest part of the breathing cycle and, thus, the related attenuation map was expected to be more similar to the respiration-averaged attenuation map. Variability in the lesion centroid shift was increased in higher diaphragm motions and was greater in PET/EICT than PET/EECT. Overall, the displacement of a middle or upper lung lesion compared with PET/ACT was often less than 5 mm. Lesion displacement was most severe for lesions located near the lung base or the dome of the diaphragm. The mean displacement was decreased for larger lesion sizes and the minimum displacement amplitude was observed for upper lung lesions.

Table 2 expectedly shows the lesion volume overestimation with a threshold at 20 % maximum voxel intensity that has been increased with smaller lesion sizes and larger motion amplitudes for type 1 respiratory pattern in both PET/EICT and PET/EECT images. However, in the lower lobe region, lesion volumes are smaller than lesions in PET/AC images. Comparing stationary truth with PET/ACT, there were some negative percentage error values in the lower lobe region indicating that PET/ACT overestimated some of the lesions in this region. Combination of the lower lung lesions with the liver in larger motion amplitudes and mismatched attenuation correction could result in lesion volume overestimation based on the threshold. However, for lesions with locations other than lower lung and liver, PET/ACT shows slightly smaller errors in tumor quantification and volume measurement. PET/EECT gave slightly larger errors for lesion locations other than lower lung region and smaller errors for lesions in the lower lung region in comparison to PET/EICT.

Large biases can be introduced by the partial volume effect (PVE), when tracer uptake in small lesion is measured [57]. PVE affects tumors with diameters less than two or three times the resolution (FWHM) of the imaging system and biases quantification results [58]. However, when comparing the size of simulated lesions and their corresponding ROIs (based on the 20 % maximum voxel intensity) with the resolution of ECAT EXACT HR+ scanner [59], which is between 4.3 and 8.3 mm depending on the position in the scanner, PVE was seen not to be a major confounding factor in this study.

Comparing PET/ACT image with stationary truth, as shown in Fig. 5, the SUV_{max} error in middle and lower lobe lesions may be explained by the motion blurring and mismatched attenuation correction, especially for liver and lung lesions near the diaphragm. Therefore, the sensitivity of PET may be reduced by such an SUV underestimation, especially for lung lesions near the diaphragm, which decreases detection of lung lesions with the tumor sizes.

As shown in Fig. 6a and b, there are some positive ΔSUV_{max} values, probably due to the mismatched attenuation correction, indicating that, in some cases, respiratory motion can also result in SUV_{max} overestimation. Due to the uniformity of the attenuation factors throughout the liver, the liver lesion ΔSUV_{max} was less affected by the mismatched attenuation map, as shown in Fig. 6a. By contrast, as shown in Fig. 6b, there are greater errors in SUV_{max} for the liver lesion as the lung space was used for AC in PET/EICT. For

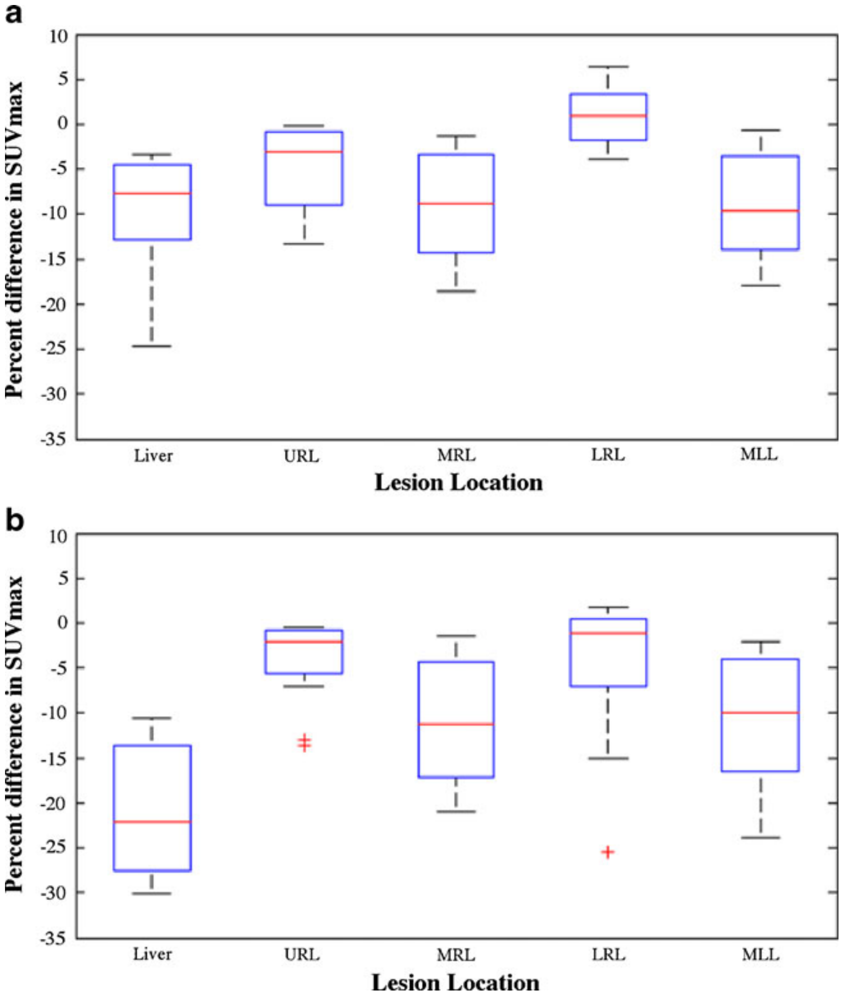

Fig. 6. *Box plots* of the ΔSUV_{max} for different lesion locations in **a** PET/EECT image compared with PET/ACT and **b** PET/EICT image compared with PET/ACT. *URL* Upper lobe in the right lung, *MRL* middle lobe in the right lung, *LRL* lower lobe in the right lung, *MLL* middle lobe in the left lung.

a lung lesion, due to the specific phase of the CTAC, if it is surrounded by the low density lung or the high density liver, an error can occur leading to undercorrection or overcorrection, respectively. For a lesion on the liver side, however, motion due to inhalation may result in undercorrection if lung is substituted for liver, but motion due to exhalation will simply substitute more liver in place of target, resulting in minimal error in the correction. As such, a target in this location is generally only subject to undercorrection and not overcorrection, while a target on the lung side suffers from both. As a consequence, when the lesion is on the higher density liver side, the AC based on EECT appears to do about the same, or even slightly better, than ACT. This does suggest that a strategy of using EECT for correction could be a reasonable approach in some situations. However, this approach would require that the target location be reliably known *a priori*, which will not generally be the case in clinical situations.

Our results also indicate that ACT results in slightly smaller errors for both tumor quantification and delineation at locations other than the lower lung region. Regardless of motion amplitude, the mean errors for upper lung lesions are less than 5 % for lesion SUV_{max}, volume, and centroid shift. Therefore, due to the relatively accurate quantification and delineation, respiratory motion compensation may not be required in PET/CT imaging of patients with upper lung lesions and a type 1 breathing pattern.

Generally, as shown in Figs. 4 and 6a and b, and Table 2, larger motion amplitude leads to greater errors in tumor quantification and delineation in terms of SUV_{max}, lesion volume, and centroid shift. However, lesions with 21- and 27-mm diameter, compared to the smaller lesions, are less sensitive to respiratory motion, which leads to smaller errors in SUV_{max} and volume measurement. Finally, no significant relation was observed between the assigned organ activity and its impact on respiratory-induced errors in lesion quantification and delineation. As the percentage threshold setting was used for lesion contouring, we believe the impact of organ activity was highly limited.

Conclusion

The aim of this study is to understand the range of respiratory-induced errors in PET/CT imaging via elaborate measurements and analysis of SUV$_{max}$, volume, and displacement for various lesions for a common patient respiratory trace with respect to the PET/ACT as a surrogate for the true values. With a complete set of lesion sizes, lesion locations, and diaphragm movements in this study, a more complete range of SUV and delineation errors for the common patient breathing pattern and different choices of attenuation map were characterized for CTAC PET images. The results indicate that respiratory motion can significantly decrease the accuracy of the PET/CT quantitative imaging, which not only has adverse implications in diagnosis but also in radiation treatment planning and treatment response monitoring, where accurate tumor volume estimation is critical [55, 56]. The results also indicate that ACT leads to slightly smaller errors in tumor quantification and delineation for lesions with locations other than lower lung region. However, there still exist volume overestimations and SUV$_{max}$ underestimations in PET/ACT imaging for some of the lesions in the lung lower lobe. Finally, we note that PET/EECT can lead to similar, even slightly smaller, errors for lower lung lesions in comparison to PET/EICT, and a strategy of using EECT for correction could be a reasonable approach in some situations. For a relatively accurate quantification and delineation, respiratory motion compensation may not be necessary in PET/CT imaging of patients with upper lung lesions and a type 1 breathing pattern.

Acknowledgments. We thank Dr. William Paul Segars for providing the XCAT phantom.

Conflict of Interest. None

References

1. Abella M, Alessio AM, Mankoff DA et al (2012) Accuracy of CT-based attenuation correction in PET/CT bone imaging. Phys Med Biol 57:2477–2490
2. Kinahan PE, Hasegawa BH, Beyer T (2003) X-ray-based attenuation correction for positron emission tomography/computed tomography scanners. Semin Nucl Med 33:166–179
3. Kinahan PE, Townsend DW, Beyer T, Sashin D (1998) Attenuation correction for a combined 3D PET/CT scanner. Medical physics 25:2046–2053
4. Ay MR, Mehranian A, Abdoli M et al (2011) Qualitative and quantitative assessment of metal artifacts arising from implantable cardiac pacing devices in oncological PET/CT studies: a phantom study. Molecular imaging and biology : MIB : the official publication of the Academy of Molecular Imaging 13:1077–1087
5. Ay MR, Shirmohammad M, Sarkar S et al (2011) Comparative assessment of energy-mapping approaches in CT-based attenuation correction for PET. Molecular imaging and biology : MIB : the official publication of the Academy of Molecular Imaging 13:187–198
6. Ay MR, Zaidi H (2006) Assessment of errors caused by X-ray scatter and use of contrast medium when using CT-based attenuation correction in PET. Eur J Nucl Med Mol Imaging 33:1301–1313
7. Erdi YE, Nehmeh SA, Pan T et al (2004) The CT motion quantitation of lung lesions and its impact on PET-measured SUVs. Journal of nuclear medicine : official publication, Society of Nuclear Medicine 45:1287–1292
8. Nehmeh SA, Erdi YE (2008) Respiratory motion in positron emission tomography/computed tomography: a review. Semin Nucl Med 38:167–176
9. Thorndyke B, Schreibmann E, Koong A, Xing L (2006) Reducing respiratory motion artifacts in positron emission tomography through retrospective stacking. Med Phys 33:2632–2641
10. Goerres GW, Burger C, Kamel E et al (2003) Respiration-induced attenuation artifact at PET/CT: technical considerations. Radiology 226:906–910
11. Kamel E, Hany TF, Burger C et al (2002) CT vs 68Ge attenuation correction in a combined PET/CT system: evaluation of the effect of lowering the CT tube current. Eur J Nucl Med Mol Imaging 29:346–350
12. Nakamoto Y, Chang AE, Zasadny KR, Wahl RL (2002) Comparison of attenuation-corrected and non-corrected FDG-PET images for axillary nodal staging in newly diagnosed breast cancer. Molecular imaging and biology : MIB : the official publication of the Academy of Molecular Imaging 4:161–169
13. Nakamoto Y, Tatsumi M, Cohade C et al (2003) Accuracy of image fusion of normal upper abdominal organs visualized with PET/CT. Eur J Nucl Med Mol Imaging 30:597–602
14. Osman MM, Cohade C, Nakamoto Y et al (2003) Clinically significant inaccurate localization of lesions with PET/CT: frequency in 300 patients. Journal of nuclear medicine : official publication, Society of Nuclear Medicine 44:240–243
15. Osman MM, Cohade C, Nakamoto Y, Wahl RL (2003) Respiratory motion artifacts on PET emission images obtained using CT attenuation correction on PET-CT. Eur J Nucl Med Mol Imaging 30:603–606
16. Beyer T, Antoch G, Blodgett T et al (2003) Dual-modality PET/CT imaging: the effect of respiratory motion on combined image quality in clinical oncology. Eur J Nucl Med Mol Imaging 30:588–596
17. Boucher L, Rodrigue S, Lecomte R, Benard F (2004) Respiratory gating for 3-dimensional PET of the thorax: feasibility and initial results. Journal of nuclear medicine : official publication, Society of Nuclear Medicine 45:214–219
18. Cohade C, Wahl RL (2003) Applications of positron emission tomography/computed tomography image fusion in clinical positron emission tomography—clinical use, interpretation methods, diagnostic improvements. Semin Nucl Med 33:228–237
19. Goerres GW, Kamel E, Heidelberg TN et al (2002) PET-CT image co-registration in the thorax: influence of respiration. Eur J Nucl Med Mol Imaging 29:351–360
20. Goerres GW, Kamel E, Seifert B et al (2002) Accuracy of image coregistration of pulmonary lesions in patients with non-small cell lung cancer using an integrated PET/CT system. Journal of nuclear medicine : official publication, Society of Nuclear Medicine 43:1469–1475
21. Pan T, Mawlawi O, Nehmeh SA et al (2005) Attenuation correction of PET images with respiration-averaged CT images in PET/CT. Journal of nuclear medicine : official publication, Society of Nuclear Medicine 46:1481–1487
22. Beyer T, Rosenbaum S, Veit P et al (2005) Respiration artifacts in whole-body (18)F-FDG PET/CT studies with combined PET/CT tomographs employing spiral CT technology with 1 to 16 detector rows. Eur J Nucl Med Mol Imaging 32:1429–1439
23. Segars WP, Mori S, Chen GTY, Tsui BMW (2007) Modeling respiratory motion variations in the 4D NCAT phantom [abstract]. 4: 2677-2679P.
24. Sarikaya I, Yeung HW, Erdi Y, Larson SM (2003) Respiratory artefact causing malpositioning of liver dome lesion in right lower lung. Clin Nucl Med 28:943–944
25. Nehmeh SA, Erdi YE, Ling CC et al (2002) Effect of respiratory gating on reducing lung motion artifacts in PET imaging of lung cancer. Medical physics 29:366–371
26. Park SJ, Ionascu D, Killoran J et al (2008) Evaluation of the combined effects of target size, respiratory motion and background activity on 3D and 4D PET/CT images. Phys Med Biol 53:3661–3679
27. Pevsner A, Nehmeh SA, Humm JL et al (2005) Effect of motion on tracer activity determination in CT attenuation corrected PET images: a lung phantom study. Medical physics 32:2358–2362
28. Papathanassiou D, Becker S, Amir R et al (2005) Respiratory motion artefact in the liver dome on FDG PET/CT: comparison of attenuation correction with CT and a caesium external source. Eur J Nucl Med Mol Imaging 32:1422–1428
29. Papathanassiou D, Liehn JC, Bourgeot B et al (2005) Cesium attenuation correction of the liver dome revealing hepatic lesion missed with computed tomography attenuation correction because of the respiratory motion artifact. Clin Nucl Med 30:120–121
30. Beyer T, Antoch G, Muller S et al (2004) Acquisition protocol considerations for combined PET/CT imaging. Journal of nuclear medicine : official publication, Society of Nuclear Medicine 45(Suppl 1):25S–35S
31. Bockisch A, Beyer T, Antoch G et al (2004) Positron emission tomography/computed tomography—imaging protocols, artifacts,

and pitfalls. Molecular imaging and biology : MIB : the official publication of the Academy of Molecular Imaging 6:188–199

32. Cook GJ, Wegner EA, Fogelman I (2004) Pitfalls and artifacts in 18FDG PET and PET/CT oncologic imaging. Semin Nucl Med 34:122–133
33. Delbeke D, Coleman RE, Guiberteau MJ et al (2006) Procedure guideline for tumor imaging with 18F-FDG PET/CT 1.0. Journal of nuclear medicine : official publication, Society of Nuclear Medicine 47:885–895
34. Zaidi H, Xu XG (2007) Computational anthropomorphic models of the human anatomy: the path to realistic Monte Carlo modeling in radiological sciences. Annu Rev Biomed Eng 9:471–500
35. Geramifar P, Ay MR, Shamsaie Zafarghandi M et al (2011) Investigation of time-of-flight benefits in an LYSO-based PET/CT scanner: a Monte Carlo study using GATE. Nuclear Instruments and Methods in Physics Research Section A: Accelerators, Spectrometers, Detectors and Associated Equipment 641:121–127
36. Geramifar P, Ay MR, Shamsaie M et al (2009) Performance comparison of four commercial GE Discovery PET/CT scanners: a Monte Carlo study using GATE. Iran J Nucl Med 17:26–33
37. Tylski P, Stute S, Grotus N et al (2010) Comparative assessment of methods for estimating tumor volume and standardized uptake value in (18)F-FDG PET. Journal of nuclear medicine : official publication, Society of Nuclear Medicine 51:268–276
38. Barret O, Carpenter TA, Clark JC et al (2005) Monte Carlo simulation and scatter correction of the GE advance PET scanner with SimSET and Geant4. Phys Med Biol 50:4823–4840
39. Zeraatkar N, Ay MR, Ghafarian P et al (2011) Monte Carlo-based evaluation of inter-crystal scatter and penetration in the PET subsystem of three GE Discovery PET/CT scanners. Nuclear Instruments and Methods in Physics Research Section A: Accelerators, Spectrometers, Detectors and Associated Equipment 659:508–514
40. Zeraatkar N, Ay MR, Kamali-Asl AR, Zaidi H (2011) Accurate Monte Carlo modeling and performance assessment of the X-PET subsystem of the FLEX triumph preclinical PET/CT scanner. Medical physics 38:1217–1225
41. Segars WP, Sturgeon G, Mendonca S et al (2010) 4D XCAT phantom for multimodality imaging research. Medical physics 37:4902–4915
42. Zubal G, Gindi G, Lee M, et al. (1990) High resolution anthropomorphic phantom for Monte Carlo analysis of internal radiation sources [abstract]. 540-547P.
43. Zaidi H, Tsui BM (2009) Review of computational anthropomorphic anatomical and physiological models. Proc IEEE 97:1938–1953
44. Ramos CD, Erdi YE, Gonen M et al (2001) FDG-PET standardized uptake values in normal anatomical structures using iterative reconstruction segmented attenuation correction and filtered back-projection. European journal of nuclear medicine 28:155–164
45. Zincirkeser S, Sahin E, Halac M, Sager S (2007) Standardized uptake values of normal organs on 18F-fluorodeoxyglucose positron emission tomography and computed tomography imaging. The Journal of international medical research 35:231–236
46. Alberts WM, American College of Chest P (2007) Diagnosis and management of lung cancer executive summary: ACCP evidence-based clinical practice guidelines (2nd Edition). Chest 132:1S–19S
47. Rivera MP, Detterbeck F, Mehta AC, American College of Chest P (2003) Diagnosis of lung cancer: the guidelines. Chest 123:129S–136S
48. Lamare F, Cresson T, Savean J et al (2007) Respiratory motion correction for PET oncology applications using affine transformation of list mode data. Phys Med Biol 52:121–140
49. Liu C, Pierce LA 2nd, Alessio AM, Kinahan PE (2009) The impact of respiratory motion on tumor quantification and delineation in static PET/CT imaging. Phys Med Biol 54:7345–7362
50. Nehmeh SA, El-Zeftawy H, Greco C et al (2009) An iterative technique to segment PET lesions using a Monte Carlo based mathematical model. Medical physics 36:4803–4809
51. Wade OL (1954) Movements of the thoracic cage and diaphragm in respiration. J Physiol 124:193–212
52. Kantarci F, Mihmanli I, Demirel MK et al (2004) Normal diaphragmatic motion and the effects of body composition: determination with M-mode sonography. Journal of ultrasound in medicine : official journal of the American Institute of Ultrasound in Medicine 23:255–260
53. Kolar P, Neuwirth J, Sanda J et al (2009) Analysis of diaphragm movement during tidal breathing and during its activation while breath holding using MRI synchronized with spirometry. Physiological research/Academia Scientiarum Bohemoslovaca 58:383–392
54. Thielemans K, Tsoumpas C, Mustafovic S et al (2012) STIR: software for tomographic image reconstruction release 2. Phys Med Biol 57:867–883
55. Han D, Yu J, Yu Y et al (2010) Comparison of (18)F-fluorothymidine and (18)F-fluorodeoxyglucose PET/CT in delineating gross tumor volume by optimal threshold in patients with squamous cell carcinoma of thoracic esophagus. Int J Radiat Oncol Biol Phys 76:1235–1241
56. Wang YC, Hsieh TC, Yu CY et al (2012) The clinical application of 4D 18F-FDG PET/CT on gross tumor volume delineation for radiotherapy planning in esophageal squamous cell cancer. J Radiat Res 53:594–600
57. Soret M, Bacharach SL, Buvat I (2007) Partial-volume effect in PET tumor imaging. Journal of nuclear medicine : official publication, Society of Nuclear Medicine 48:932–945
58. Rousset O, Rahmim A, Alavi A, Zaidi H (2007) Partial volume correction strategies in PET. PET clinics 2:235–249
59. van Velden FH, Kloet RW, van Berckel BN et al (2009) HRRT versus HR+ human brain PET studies: an interscanner test–retest study. Journal of nuclear medicine : official publication, Society of Nuclear Medicine 50:693–702